submitted to *Geophys. J. Int.*

A Unified Treatment of SKS Splitting and Surface-Wave Anisotropy for Media with Arbitrary Elastic Symmetry

Xiongwei Liu and Michael H. Ritzwoller,

Department of Physics, University of Colorado Boulder, Boulder, CO 80309, USA.

E-mail:xiongwei.liu@colorado.edu

SUMMARY

Observations of SKS splitting and surface-wave azimuthal anisotropy are two of the primary geophysical constraints on crust and upper-mantle anisotropy, yet the two methods often yield apparently inconsistent inferences about the strength and vertical extent of anisotropy. Here we show that neglecting anisotropy parameters associated with Rayleigh-Love coupling is an important and largely overlooked contributor to this discrepancy. We present a unified treatment of SKS splitting and surface-wave anisotropy. Specifically, we derive a new asymptotic expression for SKS splitting in weakly anisotropic media with arbitrary symmetry, validate it against numerical simulations, and compare it directly with quasi-degenerate surface-wave anisotropy theory. We demonstrate that the same anisotropy parameters associated with Rayleigh-Love coupling also enter SKS splitting predictions, linking the two observables within a common formalism. Because these parameters influence both observables, neglecting Rayleigh-Love coupling in surface-wave inversions can bias estimates of mantle anisotropy and lead to under-prediction of SKS splitting. Example observations from Alaska show that surface-wave inversions that account for Rayleigh-Love coupling produce stronger inferred mantle anisotropy and substantially reduce the depth extent required to explain SKS splitting, thereby helping to resolve an apparent inconsistency between surface-wave and SKS observations.

1 INTRODUCTION

SKS splitting and surface-wave azimuthal anisotropy are the two principal observational methods used to constrain mantle anisotropy, and although other approaches (e.g., Pn travel-times, shear-wave tomography, receiver-functions) also contribute, SKS and surface-waves remain the most widely used and most directly comparable indicators of anisotropy in the crust and upper mantle. Fast-axis orientations determined from the two methods are often in agreement (e.g., Feng et al., 2020; Zhu et al., 2020). Yet, despite nearly five decades of application (surface-wave azimuthal anisotropy since Forsyth (1975); shear-wave splitting since at least Crampin (1978)), the inferred magnitudes and depth distributions of anisotropy often differ markedly between the two methods. This discrepancy raises the question whether the theoretical frameworks (e.g., Montagner & Nataf, 1986; Montagner et al., 2000) commonly used to interpret SKS splitting and surface-wave anisotropy through the parameter pair $G_{c,s}$ are sufficiently complete to capture all components of the elastic tensor that influence these observables, particularly those responsible for Rayleigh-Love coupling. We show here that incorporating these additional anisotropy parameters ($M_{c,s}$, $D_{c,s}$, $K_{c,s}$) leads to substantially stronger inferred upper-mantle anisotropy and largely resolves the long-standing discrepancy between surface-wave and SKS estimates of anisotropy.

Surface-wave studies of anisotropy have advanced substantially in recent years, both in the diversity and precision of the observations and in the sophistication of the theoretical frameworks used to interpret them. Although traditionally many studies have assumed transverse isotropy with either a vertical (VTI) or horizontal (HTI) symmetry axis, recent work has included a tilt to the symmetry axis (TTI media) (e.g., Xie et al., 2015, 2017; C. Liu et al., 2024). These studies have shown that ignoring tilt can bias both the magnitude and the inferred depth distribution of anisotropy.

Historically, observational analyses of azimuthal anisotropy have focused principally on Rayleigh waves – especially the 2ψ component, where ψ is azimuth – with anisotropy models generally constructed using theory derived from Rayleigh's principle or non-degenerate perturbation theory (e.g., Smith & Dahlen, 1973; Montagner & Nataf, 1986). In contrast, new observations of both Rayleigh- and Love-wave 2ψ and 4ψ anisotropy (X. Liu et al., 2025) have been interpreted using a quasi-degenerate theory that incorporates Rayleigh-Love coupling (X. Liu & Ritzwoller, 2025), which affects the azimuthal distributions of both Rayleigh- and Love-wave phase speeds. These studies demonstrate that neglecting Love-wave azimuthal anisotropy and Rayleigh-Love coupling can significantly bias inferred anisotropy models in both amplitude and depth distribution. A principal motivation for this paper is that, as shown below, the anisotropy parameters responsible for Rayleigh-Love coupling also significantly influence SKS splitting and its interpretation.

SKS splitting measurements also provide important constraints on mantle anisotropy (e.g., Long

& Silver, 2009). Two principal measurement approaches are commonly employed: methods based on transverse-component minimization (e.g., Silver & Chan, 1991) and the splitting-intensity method (Chevrot, 2000). We focus on splitting intensity because it is robust to observational uncertainty and is directly compatible with the theoretical framework developed below.

Montagner et al. (2000) demonstrated that SKS splitting and Rayleigh-wave anisotropy are not independent observables but are principally sensitive to the same anisotropy parameters ($G_{c,s}$) under the assumptions adopted in that study. This result implies that SKS splitting can, in principle, be predicted directly from anisotropy models derived from surface-wave observations. In practice, although there is generally good agreement between the fast-axis orientations inferred from SKS splitting and Rayleigh-wave anisotropy (e.g., Lin et al., 2011; Becker et al., 2012; Feng et al., 2020; Zhu et al., 2020), significant discrepancies remain in both the magnitude (e.g., Feng et al., 2020; Zhu et al., 2020) and inferred depth distribution (e.g., Lin et al., 2011) of anisotropy. In particular, SKS splitting times predicted from surface-wave models are typically smaller – often by roughly a factor of two – than those observed. This mismatch has commonly been interpreted as evidence that a substantial fraction of SKS splitting originates from anisotropy deeper than the depth range sampled by surface-waves (e.g., Lin et al., 2011). We argue here that an important part of the discrepancy may arise because previous comparisons have focused exclusively on only one of the anisotropy parameters, $G_{c,s}$, while neglecting those associated with Rayleigh-Love coupling ($M_{c,s}, D_{c,s}, K_{c,s}$), which can significantly influence both surface-wave anisotropy and SKS splitting.

Existing comparisons between surface-wave anisotropy and SKS splitting (e.g., Montagner et al., 2000; Lin et al., 2011; Becker et al., 2012) generally neglect the effects of Rayleigh-Love coupling, which may be strong in anisotropic media that depart from VTI or HTI symmetry, including TTI and tilted orthorhombic media. Consequently, the anisotropy parameters responsible for Rayleigh-Love coupling have played only a limited role in both the surface-wave and SKS interpretations used in these comparisons. Here we extend this framework by deriving asymptotic expressions for SKS splitting in weakly anisotropic media of arbitrary symmetry and comparing them directly with the quasi-degenerate surface-wave theory of Liu & Ritzwoller (2025). We show that the same anisotropy parameters that govern Rayleigh-Love coupling in surface-waves, particularly $M_{c,s}$ and $D_{c,s}$, also contribute significantly to SKS splitting. This establishes a more complete framework for the joint interpretation of the two observables. We validate these theoretical predictions with numerical benchmarks and present observational examples from Alaska that illustrate their implications for the interpretation of seismic anisotropy.

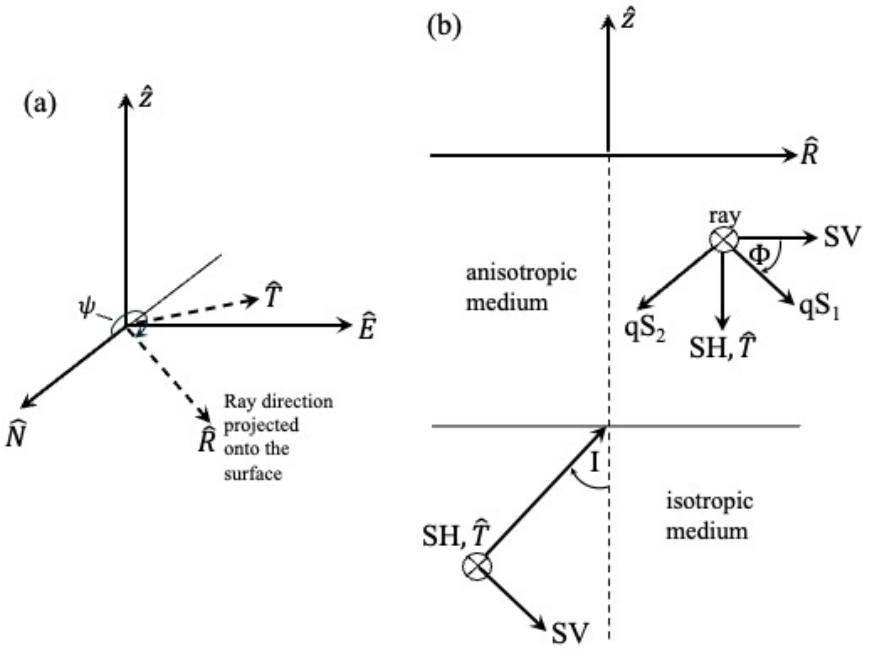

Figure 1. (a) Coordinate axes (north $\hat{N}$, east $\hat{E}$, vertical $\hat{Z}$), radial ($\hat{R}$) and transverse ($\hat{T}$) axes, and azimuthal angle (ψ), measured positive clockwise from North. (b) An SKS wave propagating in an isotropic medium is polarized in the SV direction with an incidence angle I. The SV and SH ($\hat{T}$) directions are both perpendicular to the ray. In the anisotropic medium, the ray's polarization rotates by an angle Φ and there are both quasi-S_1 and quasi-S_2 components.

2 THEORY OF SKS SPLITTING-INTENSITY IN A GENERAL ANISOTROPIC MEDIUM

2.1 Vertically homogeneous anisotropic medium

As a start, we consider an SKS wave incident on and then modified by propagation through a single homogeneous anisotropic medium – a single layer. The discussion that follows is subsequently generalized to a heterogeneous anisotropic medium (multilayers) in section 2.2.

Consider an SKS wave propagating upward in an isotropic medium in direction $\vec{n} = (\sin I \cos\psi, \sin I \sin\psi, \cos I)$ (Fig. 1), where I is the incidence angle and ψ is the azimuth. Because the initial polarization of the SKS wave lies in the SV wave direction, the vector displacement is in the plane perpendicular to $\vec{n}$:

$$\boldsymbol{u}_{VH}^{iso} = \begin{pmatrix} u_{SV}^{iso} \\ u_{SH}^{iso} \end{pmatrix} = \begin{pmatrix} u_{SV}^{iso} \\ 0 \end{pmatrix} \tag{1}$$

where u_{SV}^{iso} is the initial SKS scalar displacement in the isotropic medium. We refer to these as the $V-H$ coordinates, which lie in the transverse plane in ray-centered coordinates. The H-axis coincides with the SH direction and the V-axis with the SV direction. Following the notation of Montagner (2000), the displacement vector of the SKS wave that propagates in the isotropic medium in the $V-H$

coordinates is given by

$$u_{SV}^{iso} = a_0 e^{i\omega(t-\frac{z-z_0}{V_{iso}})} \tag{2}$$

where ω is angular frequency, z is the vertical coordinate measured positive upward from the surface (and therefore negative below the surface), and z_0 is the vertical coordinate at the base of the isotropic medium. Assuming that z lies above z_0, $z - z_0$ is positive and is the propagation distance in that isotropic medium.

Either by degenerate perturbation theory (e.g. Jech & Psencik 1989; Chen & Tromp 2007) or a variational method (Liu & Ritzwoller, 2025), when the SKS wave enters a general anisotropic medium it is split into two quasi-shear waves with polarizations rotated by angle Φ, as shown in Figure 1b, such that $V_1 = V_{iso} + \delta c_1$ and $V_2 = V_{iso} + \delta c_2$. V_1 and V_2 depend on the incidence angle I, the azimuth ψ, and the elastic tensor may have arbitrary elastic symmetry. The perturbations to the two quasi-shear wave speeds and the polarization angle Φ are determined by

$$\delta c_{1,2} = \frac{B_{11} + B_{22} \pm B}{4V_{iso}} \tag{3}$$

$$\tan 2\Phi = \frac{2B_{12}}{B_{11} - B_{22}} \tag{4}$$

where $B = \sqrt{(B_{11} - B_{22})^2 + 4B_{12}^2}$ and B_{11}, B_{22}, and B_{12} are given by equations (36)-(38) of Chen & Tromp (2007), and are functions of incidence angle I and azimuth ψ. δc_1 is the faster shear wave computed with the plus sign in front of B in equation (3) and δc_2 is the slower shear wave computed with the negative sign. There is a $\frac{\pi}{2}$ ambiguity of Φ in equation (4) because $\tan 2\Phi = \tan 2(\Phi + \frac{\pi}{2})$, so we define $2\Phi \equiv \arg[(B_{11} - B_{22}) + i\,2B_{12}] = \mathrm{atan2}(2B_{12}, B_{11} - B_{22})$.

To simplify the calculation, we define a new reference shear wave speed, V_0, as

$$V_0(\psi, I) \equiv V_{iso} + \frac{\delta c_1 + \delta c_2}{2} = V_{iso} + \frac{B_{11} + B_{22}}{4V_{iso}} \tag{5}$$

which is a function of both azimuth and incidence angle. In general, $V_0 \neq V_{iso}$. This choice removes the mean anisotropic velocity perturbation and isolates the splitting associated with the velocity difference between the quasi-shear modes. Thus, the speeds of the quasi-S_1 and quasi-S_2 waves are $V_1 = V_0 + \frac{1}{2}\delta V$ and $V_2 = V_0 - \frac{1}{2}\delta V$, respectively, where δV is the speed difference between the two quasi-shear waves

$$\delta V = \delta c_1 - \delta c_2 = \frac{B}{2V_{iso}}. \tag{6}$$

We also define a reference displacement field around which we perturb, which is polarized in the SV-direction and propagates with average phase speed V_0 in the anisotropic medium:

$$u_{SV}^{0} \equiv a_0 e^{i\omega(t-\frac{z-z_0}{V_0})} \tag{7}$$

Employing these definitions, the phase part of quasi-shear waves in the anisotropic medium can be approximated as

$$e^{i\pm} = e^{i\omega(t-\frac{z-z_0}{V_0\pm\frac{1}{2}\delta V})} \approx e^{i\omega(t-\frac{z-z_0}{V_0})} e^{\pm\frac{1}{2}i\omega\delta t} \tag{8}$$

where δt is given by

$$\delta t \equiv \frac{(z-z_0)\delta V}{V_0^2}. \tag{9}$$

In equation (8), we have applied the weak anisotropy approximation, which is accurate to first-order in $\delta V/V_0$. The expansion of phase speed assumes $\delta V/V_0 \ll 1$, while the subsequent splitting intensity approximation assumes $\omega\delta t/2 \ll 1$. The condition $\omega\delta t/2 \ll 1$ is generally more restrictive than $\delta V/V_0 \ll 1$, because splitting accumulates with propagation distance.

Based on equations (6) and (9), we could derive a fully general expression for SKS splitting time in a general one layer anisotropic medium given the definitions of B_{11}, B_{22}, and B_{12} by Chen & Tromp (2007). However, the complexity of the result would obscure both the direct theoretical comparison between SKS and surface-waves and its physical meaning. For clarity, we instead continue to apply the weak-anisotropy approximation in deriving a simpler expression for splitting intensity.

Because the two quasi-shear waves have different speeds in a general anisotropic medium, the displacement vector in $V-H$ coordinates is

$$\boldsymbol{u}_{VH} = R(\Phi)\begin{pmatrix} e^{i+} & 0 \\ 0 & e^{i-} \end{pmatrix} R(-\Phi)\boldsymbol{a_0} = \begin{pmatrix} [\cos(\frac{1}{2}\omega\delta t) + i\sin(\frac{1}{2}\omega\delta t)\cos 2\Phi]u^0_{SV} \\ [i\sin(\frac{1}{2}\omega\delta t)\sin 2\Phi]u^0_{SV} \end{pmatrix} \tag{10}$$

where $\boldsymbol{a_0} = \begin{pmatrix} a_0 \\ 0 \end{pmatrix}$ is the initial polarization of the wave as it emerges from the isotropic medium and $R(\Phi) = \begin{pmatrix} \cos\Phi & -\sin\Phi \\ \sin\Phi & \cos\Phi \end{pmatrix}$ is the 2-D rotation that defines the polarization in the anisotropic medium.

Imposing the second approximation, which is first-order in $\omega\delta t/2$, equation (10) becomes

$$\boldsymbol{u}_{VH} \approx \begin{pmatrix} u^0_{SV} + \frac{1}{2}\delta t\cos 2\Phi \dot{u}^0_{SV} \\ \frac{1}{2}\delta t\sin 2\Phi \dot{u}^0_{SV} \end{pmatrix} \tag{11}$$

where $\dot{u}^0_{SV}$ is the time derivative of u^0_{SV}. Using Φ from equation (4), δV from equation (6), and δt from equation (9), gives

$$\delta t\cos 2\Phi = \frac{(z-z_0)}{V_0^2}\cdot\frac{B}{2V_{iso}}\cdot\frac{B_{11}-B_{22}}{B} = \frac{(z-z_0)(B_{11}-B_{22})}{2V_0^2V_{iso}} \tag{12}$$

$$\delta t\sin 2\Phi = \frac{(z-z_0)}{V_0^2}\cdot\frac{B}{2V_{iso}}\cdot\frac{2B_{12}}{B} = \frac{(z-z_0)B_{12}}{V_0^2V_{iso}} \tag{13}$$

Therefore, equation (11) can be rewritten as

$$\boldsymbol{u}_{VH} \approx \begin{pmatrix} u^0_{SV} + \frac{(z-z_0)(B_{11}-B_{22})}{4V_0^2 V_{iso}}\dot{u}^0_{SV} \\ \frac{(z-z_0)B_{12}}{2V_0^2 V_{iso}}\dot{u}^0_{SV} \end{pmatrix} \approx \begin{pmatrix} u^0_{SV} + \frac{(z-z_0)(B_{11}-B_{22})}{4V_{iso}^3}\dot{u}^0_{SV} \\ \frac{(z-z_0)B_{12}}{2V_{iso}^3}\dot{u}^0_{SV} \end{pmatrix} \tag{14}$$

where we have invoked the weak anisotropy approximation in setting $V_{iso}^3 \approx V_0^2 V_{iso}$. Finally, we apply the third approximation. Because the perturbation to the SV component enters as a correction to an existing $O(1)$ displacement, whereas the SH component is itself $O(\epsilon)$ where ϵ is the characteristic fractional anisotropy, we retain only the leading-order contribution to u_{SV}:

$$\boldsymbol{u}_{VH} \approx \begin{pmatrix} u^0_{SV} \\ \frac{(z-z_0)B_{12}}{2V_{iso}^3}\dot{u}^0_{SV} \end{pmatrix} \tag{15}$$

Rotating the displacement vector $\boldsymbol{u}_{VH}$ from the $V-H$ back to the $R-T-Z$ (radial-transverse-vertical) coordinates (Fig. 1a), we obtain

$$\boldsymbol{u}_{RTZ} = \begin{pmatrix} u_R \\ u_T \\ u_Z \end{pmatrix} = \begin{pmatrix} \cos I & 0 & \sin I \\ 0 & 1 & 0 \\ -\sin I & 0 & \cos I \end{pmatrix} \begin{pmatrix} u^0_{SV} \\ \frac{(z-z_0)B_{12}}{2V_{iso}^3}\dot{u}^0_{SV} \\ 0 \end{pmatrix} = \begin{pmatrix} u^0_{SV}\cos I \\ \frac{(z-z_0)B_{12}}{2V_{iso}^3}\dot{u}^0_{SV} \\ -u^0_{SV}\sin I \end{pmatrix} \tag{16}$$

For a general anisotropic medium with an arbitrary incidence angle I and azimuth ψ, the expression for B_{12} (Chen & Tromp, 2007) is:

$$\begin{aligned} \rho B_{12}(\psi, I) =& \frac{1}{2}(\sin I + \sin 3I)(K_c \sin\psi - K_s \cos\psi) - \sin I(M_c \sin\psi + M_s \cos\psi) \\ &+ \frac{1}{2}(\cos I + \cos 3I)(G_c \sin 2\psi + G_s \cos 2\psi) + \frac{1}{8}(\cos I - \cos 3I)(B_c \sin 2\psi + B_s \cos 2\psi) \\ &- \frac{1}{4}(\cos I - \cos 3I)(H_c \sin 2\psi + H_s \cos 2\psi) - \frac{1}{4}(\sin I - 3\sin 3I)(D_c \sin 3\psi - D_s \cos 3\psi) \\ &+ \frac{1}{4}(\cos I - \cos 3I)(E_c \sin 4\psi + E_s \cos 4\psi) \end{aligned} \tag{17}$$

where expressions for the anisotropy parameters ($K_{c,s}$, $M_{c,s}$, etc) are presented in Appendix B here.

For a nearly vertically propagating SKS wave ($I \ll 1$ rad), we obtain the following approximation to equation (17):

$$\begin{aligned} \rho B_{12}(\psi, I) \quad \approx \quad & 2I(K_c \sin\psi - K_s \cos\psi) - I(M_c \sin\psi + M_s \cos\psi) \\ & + (G_c \sin 2\psi + G_s \cos 2\psi) + 2I(D_c \sin 3\psi - D_s \cos 3\psi) \end{aligned} \tag{18}$$

In the limit as $I \to 0$, only the $G_{c,s}$ contribution remains in equation (18). The $G_{c,s}$ term varies with azimuth as 2ψ. The remaining sensitivity to anisotropy is through the $K_{c,s}$, $M_{c,s}$, and $D_{c,s}$ parameters. These parameters are particularly important because they also play a central role in the description of Rayleigh-Love coupling in surface-wave theory, as discussed below. These terms are all proportional

to the incidence angle I, which is small for SKS waves. Thus, their effect on B_{12} is expected to be smaller than the $G_{c,s}$ term, but may be significant, depending on the structure of the elastic tensor. Each of these terms has an odd-order dependence on ψ. The sensitivity to the four parameters $K_{c,s}$, $M_{c,s}$, $G_{c,s}$, and $D_{c,s}$ was previously shown by Sieminski et al. (2008) based on the Born approximation. The significance of these parameters for reconciling SKS splitting and surface-wave anisotropy, however, has not previously been recognized.

Following Chevrot (2000), we define *splitting intensity* as $SI \equiv -2u_T/\dot{u}_R$ where u_T and u_R are the transverse and radial components of displacement. Therefore, using equation (16) splitting intensity is

$$SI(\psi) = -\frac{(z - z_0)B_{12}}{V_{iso}^3 \cos I} \approx -\delta t \sin 2\Phi \tag{19}$$

where again we have invoked the weak anisotropy approximation when setting $V_{iso}^3 \approx V_0^2 V_{iso}$ in equation (13) and near vertical incidence in setting $\cos I \approx 1$.

Equations (18) and (19) describe the behavior of splitting intensity in a homogeneous anisotropic layer with arbitrary elastic symmetry for a nearly vertically propagating SKS wave and provide the foundation for the multilayer generalization developed below. They show that splitting intensity depends not only on the classical $G_{c,s}$ parameters but also on $K_{c,s}$, $M_{c,s}$, and $D_{c,s}$. In earlier studies, such as Montagner et al. (2000), expressions presented for δt and Φ depended only on $G_{c,s}$ parameters and not the others that appear in equation (18). Equations (18) and (19) show that the same anisotropy parameters that influence Rayleigh-Love coupling in surface-wave theory also contribute to SKS splitting. This common dependence provides the foundation for the unified treatment of SKS splitting and surface-wave anisotropy developed in the remainder of the paper.

2.2 Vertically heterogeneous anisotropic medium

To generalize the single-layer results to a vertically heterogeneous anisotropic medium, we divide the medium into n homogeneous anisotropic layers and then take the continuum limit. We follow the approach of Montagner et al. (2000), from which we obtain

$$\boldsymbol{u}_{VH} = R_n H_n R_n^{-1} \cdot \cdots \cdot R_2 H_2 R_2^{-1} R_1 H_1 R_1^{-1} \boldsymbol{a_0} \tag{20}$$

where $R_n = R(\Phi_n)$, $R_n^{-1} = R(-\Phi_n)$, and $H_n = \begin{pmatrix} e_n^{i+} & 0 \\ 0 & e_n^{i-} \end{pmatrix}$.

Expanding the matrix product in equation (20) to second order in $\omega\delta t$ and collecting terms, we

obtain the following:

$$\boldsymbol{u}_{VH} \approx \begin{pmatrix} u^0_{SV} + \sum_{i=1}^{i=n} \frac{i\omega\delta t_i}{2} \cos 2\Phi_i u^0_{SV} - \omega^2 \sum_{i=1}^{i=n} \sum_{j=i}^{j=n} \frac{\delta t_i}{2} \frac{\delta t_j}{2} \cos 2(\Phi_j - \Phi_i) u^0_{SV} \\ \sum_{i=1}^{i=n} \frac{i\omega\delta t_i}{2} \sin 2\Phi_i u^0_{SV} - \omega^2 \sum_{i=1}^{i=n} \sum_{j=i+1}^{j=n} \frac{\delta t_i}{2} \frac{\delta t_j}{2} \sin 2(\Phi_j - \Phi_i) u^0_{SV} \end{pmatrix} \tag{21}$$

Retaining terms only to first order in $\omega\delta t$ and using $i\omega u^0_{SV} = \dot{u}^0_{SV}$, equation (21) reduces to

$$\boldsymbol{u}_{VH} \approx \begin{pmatrix} u^0_{SV} + \sum_{i=1}^{i=n} \frac{1}{2} \delta t_i \cos 2\Phi_i \dot{u}^0_{SV} \\ \sum_{i=1}^{i=n} \frac{1}{2} \delta t_i \sin 2\Phi_i \dot{u}^0_{SV} \end{pmatrix} \tag{22}$$

where $\delta t_i \cos 2\Phi_i$ and $\delta t_i \sin 2\Phi_i$ are defined by equations (12) and (13), respectively.

Using the same definition of splitting intensity introduced in the single-layer case (equation (18) combined with (19)) and taking the continuum limit by replacing the summation over layers by a depth integral, we obtain splitting intensity for a multilayer model:

$$\begin{aligned} SI &\approx -\int (\delta t \sin 2\Phi) dz \\ &= -\int \frac{dz}{\rho V^3_{iso}} [2I(K_c \sin\psi - K_s \cos\psi) - I(M_c \sin\psi + M_s \cos\psi) + \\ &\qquad + (G_c \sin 2\psi + G_s \cos 2\psi) + 2I(D_c \sin 3\psi - D_s \cos 3\psi)] \end{aligned} \tag{23}$$

Here, I is generally a function of depth, $I(z)$. To apply equation (23) most accurately, bending of the ray should be tracked at each interface. Equation (23) shows that, to first order in the amplitude of anisotropy and accumulated splitting, the contributions of individual layers to splitting intensity add linearly along the ray path. This linear superposition is the basis for the comparison between multilayer SKS splitting and surface-wave anisotropy models presented below.

The derivation of equation (23) from equation (22) assumes that the contributions of different layers to splitting intensity add linearly. This is only true because we discarded second-order cross terms in equation (21). Thus, equation (23) is not only first-order in anisotropy, it is first-order in accumulated splitting. This linear superposition provides the framework for predicting SKS splitting intensity directly from depth-dependent anisotropy models derived from surface-wave observations. To the best of our knowledge, the implications of this first-order linear superposition were first emphasized by Romanowicz & Yuan (2012), who argued, for example, that the order of the layering is unimportant at first order.

The assumptions made in our approach include the following. (1) We have assumed that anisotropy is weak so that $\delta V/V_0 \ll 1$, which is well established in earth materials. (2) We have also assumed that $\omega\delta t/2 \to 0$, which requires that the differential phase accumulated between the two quasi-shear waves generated as SKS propagates in an anisotropic medium is small. With a typical splitting time $\delta t \approx 1$ s and a period of 10 s, $\omega\delta t/2 \approx 0.3$. Although this quantity is not negligibly small, it remains sufficiently less than unity that the first-order approximation captures the leading-order dependence

of splitting intensity on anisotropy. The numerical benchmarks presented below demonstrate that this approximation remains accurate under realistic conditions. (3) The analysis is based on ray theory, which neglects scattering effects, such as those caused by heterogeneity in the medium. (4) Interfaces between the layers are horizontal. (5) We ignore the coupling between shear waves and P-waves, as well as P-SV conversions across horizontal interfaces. These assumptions can be relaxed by applying the first Born approximation (e.g. Chevrot 2006; Sieminski et al., 2008) and including coupling to the P-wave.

Montagner et al. (2000) and Romanowicz & Yuan (2012) also presented results for SKS splitting intensity in anisotropic media, but under more restrictive assumptions than we consider here. In Appendix D, we show their results can be derived from ours when we apply their assumptions.

2.3 Numerical benchmarks

To assess the accuracy of the asymptotic theory, we compare predictions from equations (18) and (23) with numerical simulations for both single-layer and multilayer anisotropic models. The single-layer benchmark isolates the contributions of the individual anisotropy parameters, whereas the multi-layer benchmark evaluates the theory in a model representative of anisotropy structures inferred from surface-wave observations.

To verify the dependence of equation (18) on the individual anisotropy parameters, we consider four homogeneous single-layer anisotropy models in which only one of the parameters K_c, M_c, G_c, or D_c is non-zero. These four models isolate the anisotropy parameters that play central roles in the SKS and surface-wave formalisms. Numerical splitting intensities are measured on waveforms computed using the SEM-FK hybrid method of Tong et al. (2014) and are then compared with predictions from equation (18).

The isotropic reference model consists of a single 200 km thick layer with density $\rho = 2720$ kg m^{-3}, $V_p = 5.80$ km/s, and $V_s = 3.46$ km/s. Four anisotropic perturbations to this reference model are considered, each independent of depth: Model 1, $K_c/A = 3\%$; Model 2, $M_c/A = 3\%$; Model 3, $G_c/L = 3\%$; and Model 4, $D_c/A = 3\%$, with all remaining anisotropy parameters set to zero in each case. Here, $A = \rho V_p^2$ and $L = \rho V_s^2$. For all simulations the incidence angle is fixed at $I = 10^\circ$.

Comparisons between numerical and theoretical splitting intensities are shown in Figure 2, which demonstrates that equation (18) reproduces the numerical splitting intensities with high accuracy for all four single-layer benchmarks. Agreement is particularly good for the M_c, G_c, and D_c models. A small discrepancy is observed only for Model 1, the K_c simulation. This discrepancy is likely caused by coupling between shear and compressional waves in the numerical simulations, an effect that is neglected in the asymptotic theory presented here. Although the relative amplitude of anisotropy

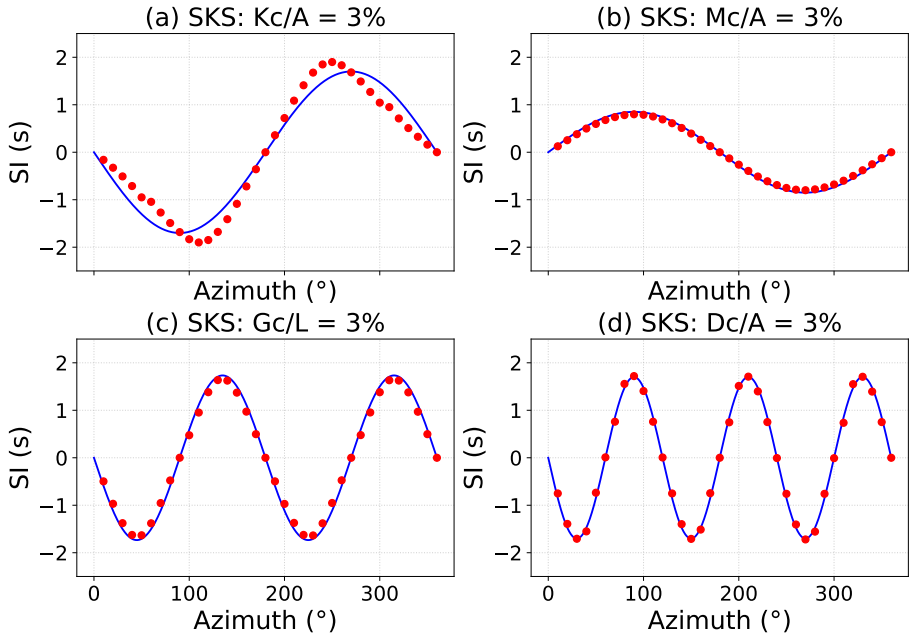

Figure 2. Single-layer numerical benchmark. Comparison is based on single-layer Models 1-4, described in the text. The blue solid line is the theoretical prediction of splitting intensity using equations 16 and (18). The red dots are numerical results from the SEM-FK hybrid method (Tong et al., 2014). (a) Model 1, (b) Model 2, (c) Model 3, and (d) Model 4. Incidence angle $I = 10°$.

is 3% in all four simulations, G_c is smallest because it is normalized by $L = \rho V_s^2$ in Figure 2, whereas K_c and M_c are normalized by $A = \rho V_p^2 > L$. For the reference model considered here, A is approximately 2.8 times larger than L.

For the multilayer benchmark, we test the asymptotic theory using a simplified but representative model of anisotropy based on models inferred from Rayleigh- and Love-wave azimuthal anisotropy across western Alaska (X. Liu and Ritzwoller, 2025, their Fig. 13; X. Liu and Ritzwoller, 2026). Those models incorporate observations of both Rayleigh- and Love-wave 2ψ and 4ψ azimuthal anisotropy and explicitly account for Rayleigh-Love coupling. The benchmark therefore provides a test of the theory closer to actual applications than the single-layer examples.

The multilayer benchmark model is TTI, with properties summarized in Figure 3. S-wave anisotropy, γ, is set to 6% in the crust and 12% in the mantle, while the dip angle is $30°$ in the crust and $40°$ in the mantle. We further assume elliptical anisotropy ($\eta_X = 4L/(A + C - 4F) = 1$, or equivalently $E = A + C - 2F - 4L = 0$), which implies $K_{c,s} = D_{c,s} = 0$ (Appendix C). Consequently, only the anisotropy parameters $G_{c,s}$ and $M_{c,s}$ are non-zero, and their depth dependence is shown in Figure 3d. The model extends to 200 km depth and is represented by 100 layers that are thinner in the crust than in the mantle.

Equation (23) reproduces both the azimuthal dependence and amplitude of splitting intensity in the

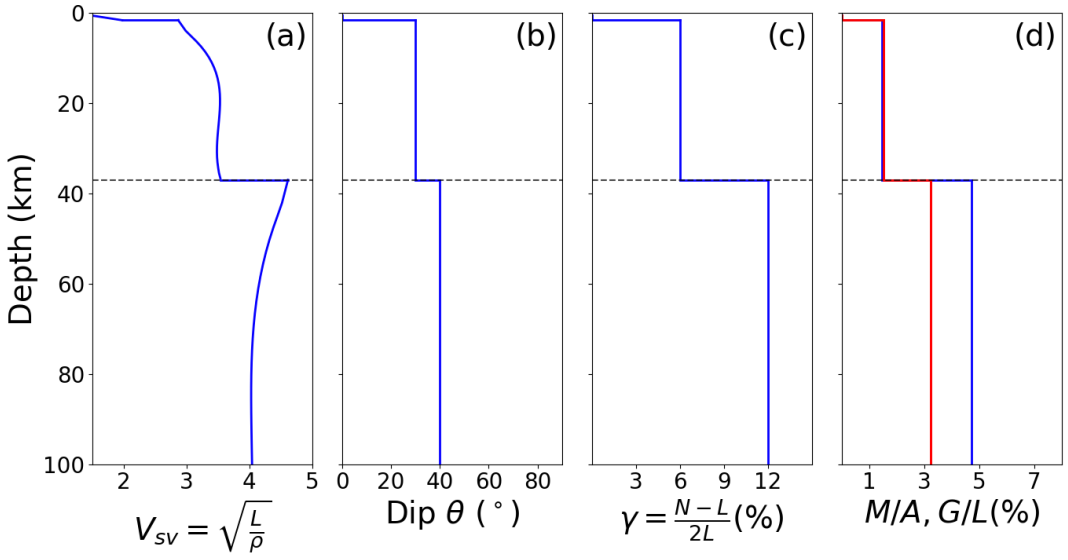

Figure 3. Aspects of the multi-layer TTI model for the numerical benchmark. Shown are (a) $\sqrt{L/\rho}$, (b) dip angle θ, (c) S-wave anisotropy $\gamma = \frac{N-L}{2L}$ here, and (d) $G = \sqrt{G_c^2 + G_s^2}$ (blue) and $M = \sqrt{M_c^2 + M_s^2}$ (red), normalized by the Love moduli L and A, respectively. This model is very similar to those presented by X. Liu and Ritzwoller (2026) for western Alaska, but is somewhat simplified and anisotropy is elliptical which implies $K_{c,s} = D_{c,s} = 0$.

multilayer model with high accuracy (Figure 4a,b). Agreement between the theoretical and numerical results is excellent over most azimuths, although the theory slightly underpredicts the peak splitting intensity. This underprediction is expected because equation (23) is accurate only to first order in anisotropy amplitude, whereas higher-order terms become increasingly important near the extrema of the splitting-intensity curve.

For vertical incidence, SKS splitting exhibits a purely 2ψ azimuthal variation. In contrast, for non-vertical incidence ($I = 10^\circ$), an additional 1ψ contribution becomes apparent. The benchmark therefore demonstrates that the asymptotic theory accurately captures both the amplitude and azimuthal dependence of SKS splitting in realistic anisotropic models, while also illustrating the importance of non-vertical-incidence terms that are absent from simpler descriptions.

3 DISCUSSION OF SURFACE-WAVE THEORY AND THE SKS FORMALISM

A principal thesis of this study is that the anisotropy parameters governing the coupling between Rayleigh and Love waves also control SKS splitting. This connection provides the basis for the unified treatment of SKS splitting and surface-wave anisotropy presented here and implies that the two observables should be interpreted jointly when constraining the elastic tensor. To clarify this connec-

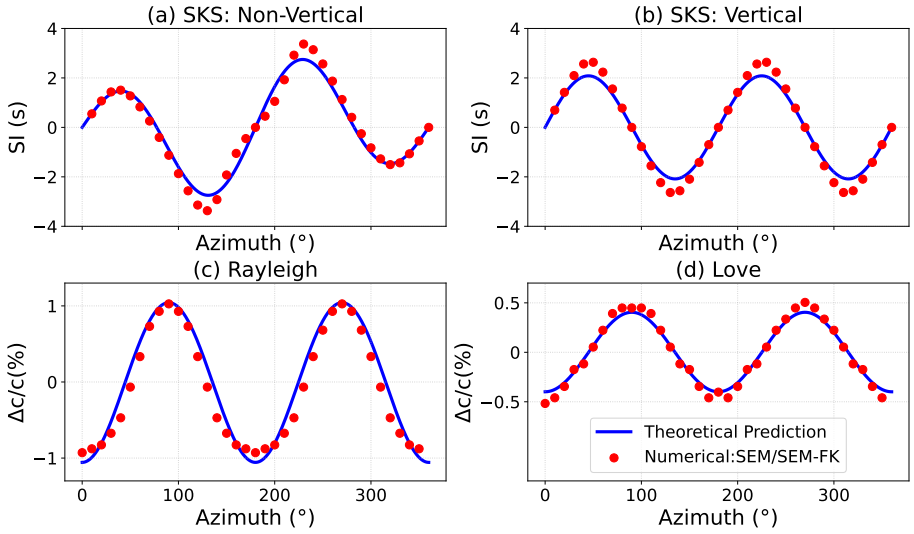

Figure 4. Multiple-layer numerical benchmark. Comparison is based on the multiple-layer model described in the text and shown in Figure 3. (a)-(b) Comparison is for splitting intensity. The blue solid line is the theoretical prediction of SKS splitting intensity using equation 23. Red dots are numerical results from the SEM-FK hybrid method (Tong et al., 2014) Non-vertical incidence is for $I = 10°$. (c)-(d) Theoretical versus numerical azimuthal variations of quasi-Rayleigh and quasi-Love phase speed at 50 s period. The blue line is the theoretical prediction using the theory of X. Liu and Ritzwoller (2025) (Appendix A here) and the red dots are from SPECFEM (Komatitsch & Tromp, 1999).

tion, we briefly review the quasi-degenerate surface-wave theory of X. Liu & Ritzwoller (2025) and compare it with the SKS formalism developed here.

A quasi-degenerate theory for the effect of anisotropy with arbitrary symmetry on surface-wave phase speeds and polarizations was presented by X. Liu & Ritzwoller (2025) and is summarized briefly in Appendix A. In a laterally homogeneous isotropic reference model, Rayleigh and Love waves propagate independently and are polarized in the vertical plane and transverse directions, respectively. Introducing anisotropy with sufficient strength and low symmetry couples Rayleigh and Love waves, producing quasi-Rayleigh and quasi-Love waves whose polarizations are rotated relative to those in the reference medium. Transversely isotropic media with either a vertical (VTI) or horizontal (HTI) symmetry axis do not couple Rayleigh and Love waves or alter their polarizations strongly. HTI media do produce azimuthal anisotropy, however, with Rayleigh-wave phase speeds displaying predominantly a 2ψ pattern and Love waves a 4ψ pattern (Montagner and Nataf, 1986). For tilted transverse isotropy (TTI) or lower-symmetry anisotropy, Rayleigh-Love coupling modifies these patterns, introducing a 2ψ component in Love waves and a 4ψ component in Rayleigh waves.

We use the same multilayer anisotropic model as in the numerical benchmark, aspects of which are shown in Figure 3, to compute the azimuthal variation of quasi-Rayleigh and quasi-Love waves,

shown in Figure 4c,d. Predictions from the theory of X. Liu and Ritzwoller (2025) are compared with numerical calculations from SPECFEM3D at a period of 50 s. As expected, the quasi-Rayleigh wave exhibits a dominant 2ψ azimuthal pattern. The quasi-Love wave, however, also displays a strong 2ψ variation, which is not expected in the absence of significant Rayleigh-Love coupling. The observation of a strong 2ψ component in Love-wave azimuthal anisotropy therefore provides compelling evidence for strong Rayleigh-Love coupling.

The connection between surface-wave anisotropy and SKS splitting arises in part because the Rayleigh-Love coupling integral X depends primarily on the anisotropy parameters $D_{c,s}$, $M_{c,s}$, and $K_{c,s}$, three of the four parameter pairs that control splitting intensity for nearly vertically propagating SKS waves (eq. (18)); the fourth is $G_{c,s}$. The coupling integral X also depends on $J_{c,s}$, which does not appear in the SKS formalism because coupling between S and P waves is neglected. The parameters $D_{c,s}$ and $M_{c,s}$ are particularly important for Rayleigh-Love coupling, whereas $K_{c,s}$ is more significant for coupling to higher modes. The parameter pair $G_{c,s}$ does not enter the X-integral, but plays an important role in surface-wave anisotropy through the A-, B-, and E-integrals, particularly through the B-integral. In the absence of Rayleigh-Love coupling (integrals $E = X = 0$), the B-integral governs the azimuthal dependence of Rayleigh-wave phase speeds.

Although the same anisotropy parameters enter both formalisms, their effect on the azimuthal variation of the two observables differs. Some parameters generate 1ψ and 3ψ variations in SKS splitting intensity while contributing primarily to 2ψ and 4ψ azimuthal variations in surface-wave phase speeds (X. Liu & Ritzwoller, 2025). Strong Rayleigh-Love coupling therefore implies that anisotropy parameters beyond $G_{c,s}$ are important. This conclusion is consistent with the presence of azimuthal variations in SKS splitting beyond the familiar 2ψ component.

The fast directions inferred from SKS splitting and quasi-Rayleigh waves are expected to align closely when Rayleigh-Love coupling is weak; that is, when the $D_{c,s}$ and $M_{c,s}$ parameters are small. In this limit, both observables are controlled primarily by the $G_{c,s}$ parameters. Equation (18) shows that the SKS fast direction depends principally on $G_{c,s}$, while equation (A.3) indicates that the B-integral, which governs Rayleigh-wave anisotropy in the absence of coupling, is also controlled by $G_{c,s}$. As the magnitudes of $D_{c,s}$ and $M_{c,s}$ increase, however, SKS splitting develops significant odd-harmonic (1ψ, 3ψ) contributions and quasi-Rayleigh-wave anisotropy may rotate away from the direction determined solely by G_c and G_s.

When SKS waves depart from purely vertical incidence, both the amplitude and azimuthal variation of splitting become strongly dependent on the $D_{c,s}$ and $M_{c,s}$ parameters that also control Rayleigh-Love coupling. Observations of SKS splitting therefore constrain Rayleigh-Love coupling, and observations of Rayleigh-Love coupling constrain SKS splitting. The two observables are consequently

strongly linked and, when interpreted jointly, provide stronger constraints on the elastic tensor than either data set alone.

Another consequence of this dependence on multiple anisotropy parameters is that SKS splitting and surface-wave azimuthal anisotropy do not necessarily need to coexist. For example, when $G_{c,s} = 0$ but $M_{c,s} \neq 0$, strong surface-wave azimuthal anisotropy may be present even when SKS splitting is weak. Conversely, when both $G_{c,s}$ and $M_{c,s}$ are nonzero, Rayleigh-wave 2ψ azimuthal anisotropy may be effectively canceled by Rayleigh-Love coupling. In this case, SKS splitting may be present even when Rayleigh-wave azimuthal anisotropy is weak or absent. Both scenarios contradict previous theoretical analyses suggesting that SKS splitting and surface-wave azimuthal anisotropy must coexist because they are both controlled by the $G_{c,s}$ parameters, and therefore provide a possible explanation for their non-coexistence in real seismic observations (e.g. Zhu et al. 2020; Tao and Li 2025). We also note that neglecting Rayleigh-Love coupling can bias SKS fast-axis predictions or lead to an overestimation of SKS splitting, as in the example shown in Figure 8 of X. Liu and Ritzwoller (2025). However, this behavior is not what is commonly observed.

In summary, the anisotropy parameters that produce strong Rayleigh-Love coupling, as observed across Alaska (e.g., X. Liu & Ritzwoller, 2025; X. Liu et al., 2025), also exert an important influence on SKS splitting. The widespread occurrence of strong 2ψ Love-wave anisotropy across Alaska indicates that the parameters $D_{c,s}$, $M_{c,s}$, and to a lesser extent $K_{c,s}$ cannot be neglected when interpreting SKS observations. These parameters, together with $G_{c,s}$, should therefore be included in calculations of SKS splitting intensity whenever evidence for significant Rayleigh-Love coupling exists. The theory presented here provides the framework for such joint interpretation.

4 OBSERVATIONAL EXAMPLES

We first examine how including Rayleigh-Love coupling in surface-wave inversions alters the inferred crustal and mantle anisotropy and the resulting predictions for SKS splitting. We begin with Point A in Figure 8a as a representative example and then extend the analysis to five locations distributed across Alaska.

X. Liu et al. (2025) present observations of the azimuthal anisotropy of Rayleigh and Love waves across Alaska, including Rayleigh- and Love-wave 2ψ and 4ψ observations. A strong Love-wave 2ψ component to anisotropy indicates significant Rayleigh-Love coupling. An example of observations of surface-wave azimuthal anisotropy is shown in Figure 5 for point A, which is identified in Figure 8a. Based on these data, X. Liu and Ritzwoller (2026) present a model of anisotropy in the crust and uppermost mantle to a depth of 200 km across Alaska, which is TTI in the crust and tilted orthorhombic (TO) in the mantle. Their inversion includes Rayleigh-Love coupling. They adopt an orthorhombic

mantle because it fits the data better, particularly Rayleigh wave 4ψ, and requires a smaller amplitude of anisotropy than a TTI model.

Examples of four of the anisotropy parameters from the model of X. Liu and Ritzwoller (2026) at point A are shown in Figure 6 with blue lines. At this point, the strike angle ϕ of anisotropy is non-zero, so both parameters of each pair may be non-zero; e.g., both G_c and G_s. Figure 6 presents the square root of the sum of the squares of each pair; e.g., $G = \sqrt{G_c^2 + G_s^2}$.

The largest parameters in this model in the mantle are G and M. K and D are usually smaller because the ellipticity parameter E is typically small. As shown in Appendix C, as E diminishes, the K and D parameters approach zero whereas M/L and G/L become proportional to the strength of S-wave anisotropy, γ. Formally, we define γ as

$$\gamma = \frac{\max C_{ij} - \min C_{ij}}{\max C_{ij} + \min C_{ij}} \tag{24}$$

where $\max C_{ij}$ is equal to the maximum of the unrotated elastic tensor components C_{44}, C_{55}, and C_{66} and $\min C_{ij}$ is the minimum of those components. For example, for a TTI medium, the maximum and minimum of those components typically are N and L, respectively, so $\gamma = (N - L)/(N + L) \approx (N - L)/2L$, which is one of the Thomsen parameters (Thomsen, 1986).

For comparison, Figure 6 also presents the four anisotropy parameters at point A in the anisotropy model of C. Liu and Ritzwoller (2024). This model is based on observations of Rayleigh-wave 2ψ anisotropy and isotropic Love-wave phase speed, with both the crust and mantle modeled as TTI. Observations of Love-wave 2ψ and 4ψ anisotropy and Rayleigh-wave 4ψ anisotropy were not included in their inversion, and Rayleigh-Love coupling was not modeled. The amplitudes of all four anisotropy parameters are smaller in the mantle than those in the model of X. Liu and Ritzwoller (2026), particularly G and M. As seen in Figure 5, the Rayleigh-wave 2ψ observations can be fit by the model of C. Liu and Ritzwoller (2024), but the remaining observations of anisotropy cannot. Those observations cannot be explained by this model and are indicative of significant Rayleigh-Love coupling. In contrast, both the Rayleigh-wave and Love-wave 2ψ and 4ψ components of azimuthal anisotropy are fit by the model of X. Liu and Ritzwoller (2026), which includes Rayleigh-Love coupling. Table 1 illustrates that including Rayleigh-Love coupling increases inferred mantle anisotropy substantially, from an average of 3.9% to 10.2% at the five locations considered.

Including Rayleigh-Love coupling, therefore, allows the azimuthal variations of both Rayleigh and Love waves to be interpreted accurately. We now examine how these differences in inferred anisotropy affect predictions of SKS splitting intensity. The azimuthal variation of SKS splitting intensity computed at point A using the model of X. Liu and Ritzwoller (2026) is shown with the blue line in Figure 7. Computations based on the model of C. Liu and Ritzwoller (2024) are shown with the red line. The

Table 1. Amplitude of S-wave anisotropy γ at 100 km depth at selected points.

Point	Coordinates (X, Y)	X. Liu and Ritzwoller (2026) (%)	C. Liu and Ritzwoller (2024) (%)
A	(147°, 64.0°)	8.8	5.3
B	(155°, 62.0°)	8.6	3.8
C	(142°, 65.5°)	11.5	3.2
D	(141°, 62.0°)	11.7	2.6
E	(155°, 66.5)	10.5	4.6
Average	–	10.2	3.9

model produced with Rayleigh-Love coupling predicts nearly twice the SKS splitting intensity as the model produced without coupling, consistent with its larger inferred mantle anisotropy (Table 1).

To assess whether the conclusions drawn at point A are representative, we examine five locations distributed across Alaska where both SKS observations and strong Love-wave 2ψ anisotropy are observed. Because strong Love-wave 2ψ anisotropy is observed widely across Alaska at mantle-sensitive periods, we expect the conclusions drawn at point A to apply broadly across Alaska. The SKS observations are from Venereau et al. (2019), but we average all measurements within a 200 km radius of

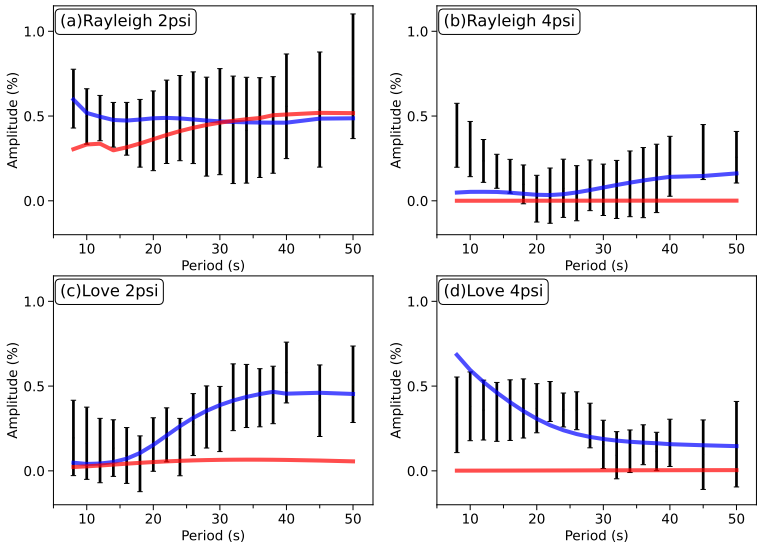

Figure 5. surface-wave observations (error bars) of Rayleigh and Love wave 2ψ and 4ψ azimuthal anisotropy at point A identified in Figure 8a. Blue line: prediction from the anisotropy model of X. Liu and Ritzwoller (2026), in which Rayleigh-Love coupling is considered in its construction. Red line: prediction from the anisotropy model of C. Liu and Ritzwoller (2024), which is constructed without considering Rayleigh-Love coupling.

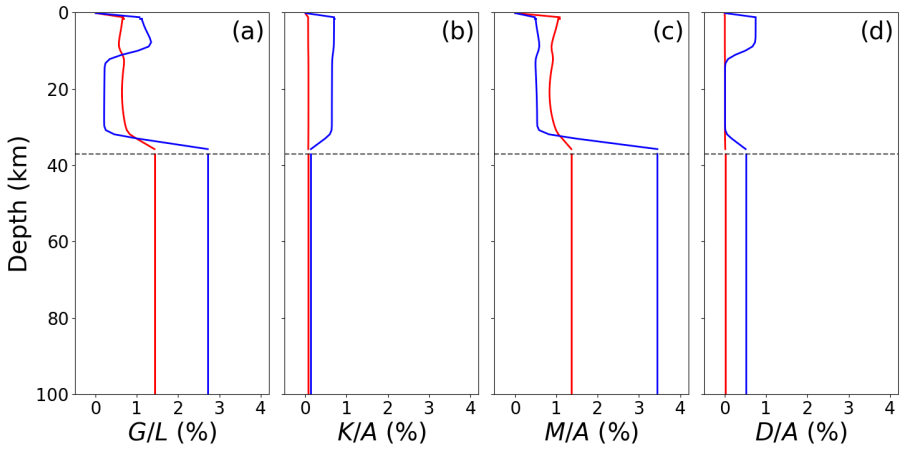

Figure 6. Examples of anisotropy parameters computed from the models of (blue lines) X. Liu and Ritzwoller (2026) and (red lines) C. Liu and Ritzwoller (2024). Each parameter-pair ($G_{c,s}, K_{c,s}, M_{c,s}, D_{c,s}$) is combined and normalized by a Love parameter (L or A); e.g., $G = \sqrt{G_c^2 + G_s^2}$.

each location. This approach ensures that approximately 10 observations contribute to the final estimate at each location and allows us to estimate error bars, whose half-width is equal to the standard deviation of the observations.

A comparison of the predictions from the two models reveals that the critical distinction between them lies not in their predictions of SKS fast-axis orientation but in their predictions of splitting intensity. As shown in Figure 8b, the models of C. Liu and Ritzwoller (2024) and X. Liu and Ritzwoller (2026) both fairly well reproduce the observed SKS fast-axis orientations. Rayleigh-Love coupling often does not need to be included for surface-wave models to predict SKS fast-axis orientations accurately. However, Rayleigh-Love coupling substantially affects the inferred strength of mantle anisotropy and, consequently, the predicted splitting intensity, as shown in Figure 8c. These results are summarized in Table 2. The model of C. Liu and Ritzwoller (2024), which neglects Rayleigh-Love coupling, systematically under-predicts SKS splitting intensity, whereas the model of X. Liu and Ritzwoller (2026), which includes Rayleigh-Love coupling, reproduces the observed splitting intensities. Both models possess anisotropy that extends to 200 km depth. The under-prediction of splitting intensity by the model that neglects Rayleigh-Love coupling reflects its weaker inferred mantle anisotropy and not an incorrect fast-axis orientation.

These examples from Alaska demonstrate that incorporating Rayleigh-Love coupling into the interpretation of surface-wave anisotropy increases the inferred strength of upper-mantle anisotropy and yields SKS splitting predictions that agree with observations. They indicate that the apparent discrepancy between surface-wave and SKS estimates of anisotropy can be largely resolved without requiring anisotropy to extend substantially below 200 km depth, at least beneath Alaska. Other continents may

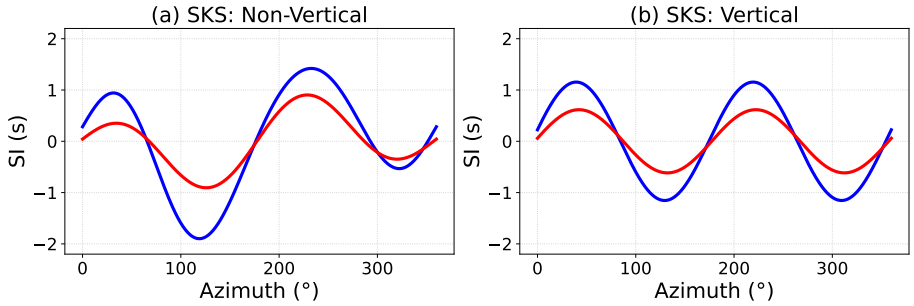

Figure 7. Examples of the azimuthal variation of the splitting intensity computed from the models of (blue lines) X. Liu and Ritzwoller (2026) and (red lines) C. Liu and Ritzwoller (2024) using the theory presented here. (a) Inclination angle $I = 10°$. (b) Inclination angle $I = 0°$.

be different, although numerous studies at both global and regional scales have reported that anisotropy inferred from surface-waves is too weak to explain observed SKS splitting (e.g., Becker et al., 2012; Feng et al., 2020; Zhu et al., 2020), leading to the inference that significant anisotropy resides in the deeper mantle (e.g., Yuan et al., 2011; Lin et al., 2011). The results presented here suggest that at least part of this discrepancy may instead arise from neglecting Rayleigh-Love coupling in surface-wave inversions. More generally, wherever a strong Love-wave 2ψ component of azimuthal anisotropy indicates significant Rayleigh-Love coupling, SKS splitting and surface-wave anisotropy should be interpreted jointly rather than used separately to constrain mantle structure. The results presented here provide a framework for such a unified interpretation.

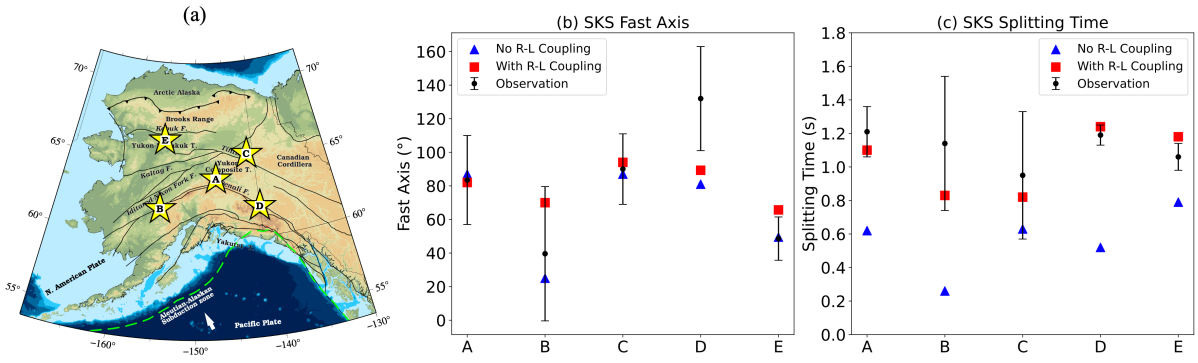

Figure 8. (a) The location of the five example locations A-E. (b) Comparison of observed SKS (b) fast-axis orientation and (c) splitting time at the five locations with predictions from the crustal and uppermost mantle anisotropy models of X. Liu & Ritzwoller (2026) and C. Liu & Ritzwoller (2024), constructed with and without considering Rayleigh-Love coupling, respectively. Both models fit SKS fast-axis orientation. Including Rayleigh-Love coupling in the inversion allows the SKS split time to be fit. (Data are summarized in Table 2.)

Table 2. SKS splitting observations and predictions from models derived from surface-wave observations.

	Pt A (9)	Pt B (10)	Pt C (11)	Pt D (21)	Pt E (8)
δt_{obs} (s)	1.21 ± 0.15	1.14 ± 0.40	0.95 ± 0.38	1.19 ± 0.06	1.06 ± 0.08
$\delta t^{\dagger}$ (s)	0.62	0.26	0.63	0.52	0.79
$\delta t^{\dagger\dagger}$ (s)	1.10	0.83	0.82	1.24	1.18
ψ_{obs} (°)	83.5 ± 26.5	39.6 ± 40	90 ± 21	132 ± 31	48.6 ± 12.9
$\psi^{\dagger}$ (°)	87	30	87	81	49.5
$\psi^{\dagger\dagger}$ (°)	82	70	94	89.3	65.7

† – SI and fast-azimuths from model of C. Liu and Ritzwoller (2024), without Rayleigh-Love coupling .

†† – SI and fast-azimuths from model of X. Liu and Ritzwoller (2026), with Rayleigh-Love coupling.

5 CONCLUSION

SKS splitting and surface-wave anisotropy are two of the principal observational constraints on seismic anisotropy in the crust and upper mantle. For decades, however, comparisons between these observables have revealed an apparent inconsistency. Although fast-axis orientations inferred from SKS splitting and surface-waves are often observed to be similar, anisotropy models derived from surface-wave observations have typically predicted SKS splitting intensities that are substantially smaller than those observed. This discrepancy has commonly been interpreted as evidence that a significant fraction of SKS splitting originates from anisotropy at depths greater than those sampled by surface-waves, providing one of the principal arguments for the existence of anisotropy below the uppermost mantle.

In this study, we present a unified treatment of SKS splitting and surface-wave anisotropy for media with arbitrary elastic symmetry. We derive a new asymptotic theory for SKS splitting in weakly anisotropic media and compare it directly with the quasi-degenerate theory of surface-wave anisotropy that includes Rayleigh-Love coupling. This comparison reveals that the two observables are linked through a common set of anisotropy parameters. Our results lead to two principal conclusions.

First, SKS splitting and surface-wave anisotropy depend on a common set of anisotropy parameters. In particular, the parameters $M_{c,s}$ and $D_{c,s}$, which govern Rayleigh-Love coupling in surface-wave theory, also contribute significantly to SKS splitting intensity. Because these parameters generate Love-wave 2ψ and Rayleigh-wave 4ψ anisotropy, observations of these signals provide evidence that they may also contribute significantly to SKS splitting. Because both data sets constrain overlapping but distinct combinations of anisotropy parameters, their joint interpretation provides stronger constraints on the strength, geometry, and depth distribution of anisotropy than either observable alone.

Second, Rayleigh-Love coupling of surface-waves plays a central role in the comparison between SKS splitting and surface-wave anisotropy. Surface-wave inversions that incorporate Rayleigh-

Love coupling produce substantially stronger anisotropy in the uppermost mantle than inversions that neglect coupling. In the Alaska examples presented here, the resulting increase in anisotropy strength brings predicted SKS splitting intensities into agreement with observations without requiring anisotropy to extend below the uppermost mantle (200 km depth). These results indicate that neglecting Rayleigh-Love coupling in surface-wave inversions can contribute significantly to the long-standing discrepancy between SKS splitting and surface-wave anisotropy.

The results we present for Alaska may turn out not to represent continental structure in general. However, observations of Love-wave 2ψ and Rayleigh-wave 4ψ azimuthal anisotropy have been reported in other regions, both at global (e.g., Montagner & Tanimoto, 1990; Trampert & Woodhouse, 2003; Ekström, 2011) and regional scales (e.g., Weeraratne et al., 2007; Polat et al., 2012; Zigone et al., 2015; Russell et al., 2019). Thus, in regions where strong Love-wave 2ψ or Rayleigh-wave 4ψ anisotropy is observed, previous inferences of deep-mantle anisotropy based on discrepancies between surface-wave and SKS observations may warrant reexamination.

More broadly, the framework developed here provides a basis for the joint interpretation and eventual joint inversion of SKS splitting together with Rayleigh- and Love-wave azimuthal anisotropy. Because these observables depend on overlapping but distinct combinations of anisotropy parameters, their combined analysis offers the prospect of substantially improved constraints on the strength, geometry, and depth distribution of seismic anisotropy in the crust and upper mantle.

Acknowledgements

We are very grateful to Yu Chen for invaluable assistance in setting up the numerical simulations for surface-waves and SKS splitting. We also thank Chuanming Liu for providing the depth-dependent elastic tensor model beneath Alaska (C. Liu & Ritzwoller 2024). We greatly appreciate help from IRIS Data Services, which are funded through the Seismological Facilities for the Advancement of Geoscience and EarthScope (SAGE) Proposal of the National Science Foundation under Cooperative Agreement EAR-1851048. Aspects of this research were supported by EAR-1928395 and EAR-1952209 at the University of Colorado Boulder.

Data Availability Statement

Original seismic waveform data were obtained from the Data Management Center of IRIS (www.iris.edu). The complete surface-wave dataset used to generate the seismic models is publicly available on Zenodo (X. Liu, 2025, https://zenodo.org/records/17118270). Seismic models based primarily on Rayleigh-wave anisotropy were taken from C. Liu and Ritzwoller (2024) and are available through the

EarthScope Earth Model Collaboration repository (https://ds.iris.edu/ds/products/emc-earthmodels/).

ObsPy (Beyreuther *et al*. 2010) is used in data processing.

REFERENCES

Becker, T. W., Lebedev, S., & Long, M., 2012. On the relationship between azimuthal anisotropy from shear wave splitting and surface wave tomography, *Journal of Geophysical Research: Solid Earth*, **117**(B1).

Beyreuther, M., Barsch, R., Krischer, L., Megies, T., Behr, Y., & Wassermann, J., 2010. Obspy: A python toolbox for seismology, *Seismological Research Letters*, **81**(3), 530–533.

Chen, M. & Tromp, J., 2007. Theoretical and numerical investigations of global and regional seismic wave propagation in weakly anisotropic earth models, *Geophysical Journal International*, **168**(3), 1130–1152.

Chevrot, S., 2000. Multichannel analysis of shear wave splitting, *Journal of Geophysical Research: Solid Earth*, **105**(B9), 21579–21590.

Chevrot, S., 2006. Finite-frequency vectorial tomography: a new method for high-resolution imaging of upper mantle anisotropy, *Geophysical Journal International*, **165**(2), 641–657.

Chevrot, S. & Van Der Hilst, R. D., 2003. On the effects of a dipping axis of symmetry on shear wave splitting measurements in a transversely isotropic medium, *Geophysical Journal International*, **152**(2), 497–505.

Crampin, S., 1978. Seismic-wave propagation through a cracked solid: polarization as a possible dilatancy diagnostic, *Geophysical Journal International*, **53**(3), 467–496.

Ekström, G., 2011. A global model of love and rayleigh surface wave dispersion and anisotropy, 25-250 s, *Geophysical Journal International*, **187**(3), 1668–1686.

Feng, L., Liu, C., & Ritzwoller, M., 2020. Azimuthal anisotropy of the crust and uppermost mantle beneath alaska, *Journal of Geophysical Research: Solid Earth*, **125**(12), e2020JB020076.

Forsyth, D. W., 1975. The early structural evolution and anisotropy of the oceanic upper mantle, *Geophysical Journal International*, **43**(1), 103–162.

Jech, J. & Pšenčík, I., 1989. First-order perturbation method for anisotropic media, *Geophysical Journal International*, **99**(2), 369–376.

Komatitsch, D. & Tromp, J., 1999. Introduction to the spectral element method for three-dimensional seismic wave propagation, *Geophysical journal international*, **139**(3), 806–822.

Lin, F.-C., Ritzwoller, M. H., Yang, Y., Moschetti, M. P., & Fouch, M. J., 2011. Complex and variable crustal and uppermost mantle seismic anisotropy in the western united states, *Nature Geoscience*, **4**(1), 55–61.

Liu, C. & Ritzwoller, M. H., 2024. Seismic anisotropy and deep crustal deformation across alaska, *Journal of Geophysical Research: Solid Earth*, **129**(5), e2023JB028525.

Liu, X. & Ritzwoller, M. H., 2025. The effect of rayleigh–love coupling in an anisotropic medium, *Geophysical Journal International*, **241**(2), 1204–1225.

Liu, X. & Ritzwoller, M. H., 2026. The elastic tensor in the crust and uppermost mantle beneath alaska from surface wave observations, *Manuscript In Preparation*.

Liu, X., Liu, C., & Ritzwoller, M. H., 2025. The characteristics of rayleigh and love wave azimuthal anisotropy: Observations across alaska, *Journal of Geophysical Research: Solid Earth*, **130**(11), e2025JB032042.

Long, M. D. & Silver, P. G., 2009. Shear wave splitting and mantle anisotropy: Measurements, interpretations, and new directions, *Surveys in Geophysics*, **30**(4), 407–461.

Montagner, J.-P. & Nataf, H.-C., 1986. A simple method for inverting the azimuthal anisotropy of surface waves, *Journal of Geophysical Research: Solid Earth*, **91**(B1), 511–520.

Montagner, J.-P. & Tanimoto, T., 1990. Global anisotropy in the upper mantle inferred from the regionalization of phase velocities, *Journal of Geophysical Research: Solid Earth*, **95**(B4), 4797–4819.

Montagner, J.-P., Griot-Pommera, D.-A., & Lavé, J., 2000. How to relate body wave and surface wave anisotropy?, *Journal of Geophysical Research: Solid Earth*, **105**(B8), 19015–19027.

Polat, G., Lebedev, S., Readman, P. W., O'Reilly, B., & Hauser, F., 2012. Anisotropic rayleigh-wave tomography of ireland's crust: Implications for crustal accretion and evolution within the caledonian orogen, *Geophysical Research Letters*, **39**(4).

Romanowicz, B. & Yuan, H., 2012. On the interpretation of sks splitting measurements in the presence of several layers of anisotropy, *Geophysical Journal International*, **188**(3), 1129–1140.

Russell, J. B., Gaherty, J. B., Lin, P.-Y. P., Lizarralde, D., Collins, J. A., Hirth, G., & Evans, R. L., 2019. High-resolution constraints on pacific upper mantle petrofabric inferred from surface-wave anisotropy, *Journal of Geophysical Research: Solid Earth*, **124**(1), 631–657.

Sieminski, A., Paulssen, H., Trampert, J., & Tromp, J., 2008. Finite-frequency sks splitting: measurement and sensitivity kernels, *Bulletin of the Seismological Society of America*, **98**(4), 1797–1810.

Silver, P. G. & Chan, W. W., 1991. Shear wave splitting and subcontinental mantle deformation, *Journal of Geophysical Research: Solid Earth*, **96**(B10), 16429–16454.

Smith, M. L. & Dahlen, F., 1973. The azimuthal dependence of love and rayleigh wave propagation in a slightly anisotropic medium, *Journal of Geophysical Research*, **78**(17), 3321–3333.

Tao, Z. & Li, A., 2025. Azimuthal anisotropy in northeastern america from joint inversion of rayleigh waves

and shear wave splitting data, *Journal of Geophysical Research: Solid Earth*, **130**(11), e2025JB031327.

Thomsen, L., 1986. Weak elastic anisotropy, *Geophysics*, **51**(10), 1954–1966.

Tong, P., Chen, C.-w., Komatitsch, D., Basini, P., & Liu, Q., 2014. High-resolution seismic array imaging based on an sem-fk hybrid method, *Geophysical Journal International*, **197**(1), 369–395.

Trampert, J. & Woodhouse, J. H., 2003. Global anisotropic phase velocity maps for fundamental mode surface waves between 40 and 150 s, *Geophysical Journal International*, **154**(1), 154–165.

Venereau, C., Martin-Short, R., Bastow, I. D., Allen, R. M., & Kounoudis, R., 2019. The role of variable slab dip in driving mantle flow at the eastern edge of the alaskan subduction margin: Insights from shear-wave splitting, *Geochemistry, Geophysics, Geosystems*, **20**(5), 2433–2448.

Weeraratne, D. S., Forsyth, D. W., Yang, Y., & Webb, S. C., 2007. Rayleigh wave tomography beneath intraplate volcanic ridges in the south pacific, *Journal of Geophysical Research: Solid Earth*, **112**(B6).

Xie, J., Ritzwoller, M. H., Brownlee, S., & Hacker, B., 2015. Inferring the oriented elastic tensor from surface wave observations: preliminary application across the western united states, *Geophysical Journal International*, **201**(2), 996–1021.

Xie, J., Ritzwoller, M. H., Shen, W., & Wang, W., 2017. Crustal anisotropy across eastern tibet and surroundings modeled as a depth-dependent tilted hexagonally symmetric medium, *Geophysical Journal International*, **209**(1), 466–491.

Yuan, H., Romanowicz, B., Fischer, K. M., & Abt, D., 2011. 3-d shear wave radially and azimuthally anisotropic velocity model of the north american upper mantle, *Geophysical Journal International*, **184**(3), 1237–1260.

Zhu, H., Yang, J., & Li, X., 2020. Azimuthal anisotropy of the north american upper mantle based on full waveform inversion, *Journal of Geophysical Research: Solid Earth*, **125**(2), e2019JB018432.

Zigone, D., Ben-Zion, Y., Campillo, M., & Roux, P., 2015. Seismic tomography of the southern california plate boundary region from noise-based rayleigh and love waves, *Pure and Applied Geophysics*, **172**(5), 1007–1032.

APPENDIX A: SURFACE-WAVE THEORY IN A GENERAL ANISOTROPIC MEDIUM

Finding the phase speeds and polarizations of coupled quasi-Rayleigh and quasi-Love waves in a general anisotropic medium can be approximated as an eigenvalue problem (X. Liu & Ritzwoller, 2025):

$$\begin{pmatrix} A & E+iX \\ E-iX & B \end{pmatrix} \begin{pmatrix} a_L^* \\ a_R^* \end{pmatrix} = \omega^2 \begin{pmatrix} a_L^* \\ a_R^* \end{pmatrix} \tag{A.1}$$

where A, B, E, and X are

$$A(\psi) = k^2 \int_0^\infty dz[(\mathcal{N} - E_c \cos 4\psi + E_s \sin 4\psi)W^2 + (\mathcal{L} - G_c \cos 2\psi + G_s \sin 2\psi)W'^2/k^2] \tag{A.2}$$

$$\begin{aligned} B(\psi) =& k^2 \int_0^\infty dz[(\mathcal{A} + B_c \cos 2\psi - B_s \sin 2\psi + E_c \cos 4\psi - E_s \sin 4\psi)V^2 \\ &+ (\mathcal{L} + G_c \cos 2\psi - G_s \sin 2\psi)(U - \frac{V'}{k})^2 \\ &+ 2(\mathcal{F} + H_c \cos 2\psi - H_s \sin 2\psi)VU'/k + \mathcal{C}U'^2/k^2] \end{aligned} \tag{A.3}$$

$$\begin{aligned} E(\psi) =& k^2 \int_0^\infty dz[(-\frac{1}{2}B_c \sin 2\psi - \frac{1}{2}B_s \cos 2\psi - E_c \sin 4\psi - E_s \cos 4\psi)WV \\ &+ (G_c \sin 2\psi + G_s \cos 2\psi)(U - \frac{V'}{k})W'/k + (-H_c \sin 2\psi - H_s \cos 2\psi)WU'/k] \end{aligned} \tag{A.4}$$

$$\begin{aligned} X(\psi) =& k^2 \int_0^\infty dz\{[2(J_c - M_c)\sin\psi - 2(J_s + M_s)\cos\psi + D_c \sin 3\psi - D_s \cos 3\psi]VW'/k \\ &+ (M_c \sin\psi + M_s \cos\psi + D_c \sin 3\psi - D_s \cos 3\psi)W(U - \frac{V'}{k}) \\ &+ 2[(J_c - K_c)\sin\psi - (J_s - K_s)\cos\psi]W'U'/k^2\} \end{aligned} \tag{A.5}$$

and where ψ is the wave propagation direction, k is the wavenumber, W, U and V are the surface-wave eigenfunctions, and $\mathcal{A}, \mathcal{C}, \mathcal{N}, \mathcal{L}, \mathcal{F}$, and so forth are anisotropy parameters defined in Appendix B. The solution to this eigenvalue problem gives the coupled quasi-Love and quasi-Rayleigh wave eigenfrequencies

$$\omega^2 = \frac{A + B \pm \sqrt{(A-B)^2 + 4(E^2 + X^2)}}{2} \equiv \frac{1}{2}\left[A + B \pm D\right] \tag{A.6}$$

or phase speed sgiven by

$$V^2{}_{qL} = \frac{1}{2k^2}\left[A + B + D\right] \tag{A.7}$$

$$V^2{}_{qR} = \frac{1}{2k^2}\left[A + B - D\right] \tag{A.8}$$

where

$$D \equiv ((A-B)^2 + 4(E^2 + X^2))^{1/2}. \tag{A.9}$$

In addition to ignoring finite frequency effects, eq.(A.1) only considers the coupling between one Rayleigh wave mode and one Love wave mode from a reference medium, and assumes that the surface-wave mode in the anisotropic medium can be expressed as a superposition of these two modes, ignoring the coupling to all other modes. Based on these assumptions, equation (A.1) is a first-order approximation of the exact solution, which is appropriate for many applications.

APPENDIX B: THE 21 ANISOTROPY PARAMETERS

Montagner & Nataf (1986) introduced linear recombinations of the elastic tensor components to define certain anisotropic parameters needed to analyze surface-wave azimuthal anisotropy. Chen & Tromp (2007) introduced others that also are needed for body waves. We follow Chen & Tromp (2007) by

595 including the negative sign in the definition of G_s, B_s, H_s and E_s as follows:

$$\mathcal{A} = \frac{1}{8}(3C_{11} + 3C_{22} + 2C_{12} + 4C_{66}) \tag{B.1}$$

$$\mathcal{C} = C_{33} \tag{B.2}$$

$$\mathcal{N} = \frac{1}{8}(C_{11} + C_{22} - 2C_{12} + 4C_{66}) \tag{B.3}$$

$$\mathcal{L} = \frac{1}{2}(C_{44} + C_{55}) \tag{B.4}$$

$$\mathcal{F} = \frac{1}{2}(C_{13} + C_{23}) \tag{B.5}$$

$$J_c = \frac{1}{8}(3C_{15} + C_{25} + 2C_{46}) \tag{B.6}$$

$$J_s = \frac{1}{8}(C_{14} + 3C_{24} + 2C_{56}) \tag{B.7}$$

$$K_c = \frac{1}{8}(3C_{15} + C_{25} + 2C_{46} - 4C_{35}) \tag{B.8}$$

$$K_s = \frac{1}{8}(C_{14} + 3C_{24} + 2C_{56} - 4C_{34}) \tag{B.9}$$

$$M_c = \frac{1}{4}(C_{15} - C_{25} + 2C_{46}) \tag{B.10}$$

$$M_s = \frac{1}{4}(C_{14} - C_{24} - 2C_{56}) \tag{B.11}$$

$$G_c = \frac{1}{2}(C_{55} - C_{44}) \tag{B.12}$$

$$G_s = -C_{45} \tag{B.13}$$

$$B_c = \frac{1}{2}(C_{11} - C_{22}) \tag{B.14}$$

$$B_s = -(C_{16} + C_{26}) \tag{B.15}$$

$$H_c = \frac{1}{2}(C_{13} - C_{23}) \tag{B.16}$$

$$H_s = -C_{36} \tag{B.17}$$

$$D_c = \frac{1}{4}(C_{15} - C_{25} - 2C_{46}) \tag{B.18}$$

$$D_s = \frac{1}{4}(C_{14} - C_{24} + 2C_{56}) \tag{B.19}$$

$$E_c = \frac{1}{8}(C_{11} + C_{22} - 2C_{12} - 4C_{66}) \tag{B.20}$$

$$E_s = -\frac{1}{2}(C_{16} - C_{26}) \tag{B.21}$$

596 We use the script notation for $\mathcal{A}, \mathcal{C}, \mathcal{N}, \mathcal{L}$ and $\mathcal{F}$ (using these five parameters to construct an effective
597 VTII or transversely isotropic medium) to distinguish them from the Love moduli A, C, N, L and
598 F that define the reference VTI medium that is the basis for the elastic tensor for a TTI medium in
599 Appendix A.

600 J_c (J_s), K_c (K_s) and M_c (M_s) are body wave 1ψ azimuthal anisotropy parameters and D_c (D_s)
601 is the body wave 3ψ azimuthal anisotropy parameter, which were not included by Montagner &

Nataf (1986). G_c (G_s), B_c (B_s) and H_c (H_s) are 2ψ azimuthal anisotropic parameters for both body waves and surface-waves. E_c (E_s) is the 4ψ azimuthal anisotropic parameter for both body waves and surface-waves.

For a TTI medium in which the strike of anisotropy lies along the x_1-axis, all parameters with the "s" subscript are zero, so 13 of the anisotropic parameters are non-zero, forming a medium with effective monoclinic symmetry.

APPENDIX C: THE ANISOTROPY PARAMETERS IN A TTI MEDIUM

The elastic tensor for a TTI medium (with no rotation around the vertical axis so that the strike of anisotropy lies along the x_1 axis) is presented in Appendix A of X. Liu & Ritzwoller (2025). Using these equations, the anisotropy parameters for a general TTI medium (with the dip angle θ is the rotation around y-axis and the strike angle ϕ is the rotation around z-axis) are:

$$J_c = [\frac{1}{8}E\sin\theta\cos\theta(3\sin^2\theta-2)+\frac{1}{4}(C-A)\sin\theta\cos\theta]\cos\phi \quad \text{(C.1)}$$

$$J_s = [\frac{1}{8}E\sin\theta\cos\theta(3\sin^2\theta-2)+\frac{1}{4}(C-A)\sin\theta\cos\theta]\sin\phi \quad \text{(C.2)}$$

$$K_c = [\frac{1}{8}E\sin\theta\cos\theta(7\sin^2\theta-4)]\cos\phi \quad \text{(C.3)}$$

$$K_s = [\frac{1}{8}E\sin\theta\cos\theta(7\sin^2\theta-4)]\sin\phi \quad \text{(C.4)}$$

$$M_c = [\frac{1}{4}E\sin^3\theta\cos\theta+(L-N)\sin\theta\cos\theta]\cos\phi \quad \text{(C.5)}$$

$$M_s = -[\frac{1}{4}E\sin^3\theta\cos\theta+(L-N)\sin\theta\cos\theta]\sin\phi \quad \text{(C.6)}$$

$$G_c = [\frac{1}{2}E\sin^2\theta\cos^2\theta+\frac{1}{2}(L-N)\sin^2\theta]\cos 2\phi \quad \text{(C.7)}$$

$$G_s = -[\frac{1}{2}E\sin^2\theta\cos^2\theta+\frac{1}{2}(L-N)\sin^2\theta]\sin 2\phi \quad \text{(C.8)}$$

$$B_c = [-\frac{1}{2}E\sin^2\theta\cos^2\theta+\frac{1}{2}(C-A)\sin^2\theta]\cos 2\phi \quad \text{(C.9)}$$

$$B_s = -[-\frac{1}{2}E\sin^2\theta\cos^2\theta+\frac{1}{2}(C-A)\sin^2\theta]\sin 2\phi \quad \text{(C.10)}$$

$$H_c = [\frac{1}{2}E\sin^2\theta\cos^2\theta-\frac{1}{2}(A-F-2N)\sin^2\theta]\cos 2\phi \quad \text{(C.11)}$$

$$H_s = -[\frac{1}{2}E\sin^2\theta\cos^2\theta-\frac{1}{2}(A-F-2N)\sin^2\theta]\sin 2\phi \quad \text{(C.12)}$$

$$D_c = [\frac{1}{4}E\sin^3\theta\cos\theta]\cos 3\phi \quad \text{(C.13)}$$

$$D_s = [\frac{1}{4}E\sin^3\theta\cos\theta]\sin 3\phi \quad \text{(C.14)}$$

$$E_c = [\frac{1}{8}E\sin^4\theta]\cos 4\phi \quad \text{(C.15)}$$

$$E_s = -[\frac{1}{8}E\sin^4\theta]\sin 4\phi \quad \text{(C.16)}$$

where A, C, N, L, and F are the Love moduli for the reference VTI medium which is tilted by angle θ relative to the vertical axis to produce the TTI medium and $E = A + C - 2F - 4L$.

APPENDIX D: COMPARISON WITH PREVIOUS THEORETICAL STUDIES

The theory of Montagner et al. (2000) is for an HTI medium ($\theta = 90°$) with vertical propagation ($I = 0°$). In this case, let $\rho V_{iso}^2 \approx L, \psi = \Psi, G = \sqrt{G_c^2 + G_s^2}$, $G_c = G\cos 2\Psi_G$, and $G_s = -G\sin 2\Psi_G$, as the G_s in Chen & Tromp (2007) which we follow is the opposite of the G_s in Montagner et al. (2000), from equation (23) we obtain

$$SI \approx -\sin 2\Psi \int \sqrt{\frac{\rho}{L}}\frac{G_c}{L}dz - \cos 2\Psi \int \sqrt{\frac{\rho}{L}}\frac{G_s}{L}dz = \delta\bar{t}\sin 2(\bar{\Psi} - \Psi) \tag{D.1}$$

$$\delta\bar{t} = \sqrt{\left(\int \sqrt{\frac{\rho}{L}}\frac{G_c}{L}dz\right)^2 + \left(\int \sqrt{\frac{\rho}{L}}\frac{G_s}{L}dz\right)^2} \tag{D.2}$$

$$tan2\bar{\Psi} = -\frac{\int \sqrt{\frac{\rho}{L}}\frac{G_s}{L}dz}{\int \sqrt{\frac{\rho}{L}}\frac{G_c}{L}dz} \tag{D.3}$$

Equations (D.1 - D.3) are the equations (20) - (22) in Montagner et al. (2000) with a sign difference in the definition of $\bar{\Psi}$ because the G_s in Chen & Tromp (2007) is the opposite of the G_s in Montagner et al. (2000).

The theory Romanowicz & Yuan (2012) is for a TTI medium with elliptical anisotropy. We present in Appendix C the anisotropy parameters for a TTI medium, which together with the assumption of elliptical anisotropy ($E = A + C - 2F - 4L = 0$) greatly simplify the anisotropy parameters. In this case, $K_c = K_s = D_c = D_s = E_c = E_s = 0$ and we have from equation (23):

$$SI = -\int \frac{dz}{\rho V_{iso}^3}\left[-I(M_c\sin\psi + M_s\cos\psi) + (G_c\sin 2\psi + G_s\cos 2\psi)\right] \tag{D.4}$$

Applying equations (C.5) - (C.8) to an elliptical TTI medium with dip angle θ and strike angle ϕ (defined in the Appendix C):

$$SI = \int \frac{(L-N)dz}{2\rho V_{iso}^3}\left[-\sin^2\theta\sin 2(\psi - \phi) + I\sin 2\theta\sin(\psi - \phi)\right] \tag{D.5}$$

We define the tilt angle θ positive clockwise from the vertical, whereas Romanowicz & Yuan (2012) defines it (Θ) clockwise from the horizontal. Details of the relation between θ and Θ depend on the azimuth at which Θ is defined, but for comparison here we take $\theta = \pi/2 + \Theta$. Using $\sin 2\theta = -\sin 2\Theta$, $\sin^2\theta = \cos^2\Theta$, and $\frac{(L-N)dz}{2\rho V_{iso}^3} \approx \frac{dz}{V_{iso}}\frac{G}{L} = \frac{dz}{V_{iso}}\frac{L-N}{2L} = \delta t_j$, equation (D.5) can be rewritten

in terms of Θ as

$$\begin{aligned} SI &= -\int \frac{(L-N)dz}{2\rho V_{iso}^3} \left[\cos^2\Theta \sin 2(\psi-\phi) + I \sin 2\theta \sin(\psi-\phi)\right] \\ &\approx \sum_{j=0}^{n} \delta t_j \left[\cos^2\Theta_j \sin 2(\phi_j-\psi) + \sin 2\Theta_j \sin(\phi_j-\psi)\tan I\right] \end{aligned} \tag{D.6}$$

This is the same as equation (31) of Romanowicz & Yuan (2012), with a factor of -2 due to our definition of the splitting-intensity as $SI = -2u_T/\dot{u}_R$.

We do not understand one aspect of the results obtained by Romanowicz & Yuan (2012). For vertical incidence ($I = 0^\circ$) in a TTI medium, our theory (eq. (16)) has no vertical component of displacement. Romanowicz & Yuan (2012) do obtain a vertical component even for vertical incidence as shown in the their equation (24). A vertical component can only be generated if there is a P-SV conversion across interfaces or P and S wave are coupled, which are not included in their theory or ours.

Chevrot & van der Hilst (2003) present expressions for splitting time for a general TTI medium. Because their results are not for splitting intensity we do not derive their results from ours.